






# Pseudo Quad-Pol Simulation From Compact Polarimetric SAR Data via a Complex-Valued Dual-Branch Convolutional Neural Network

Fan Zhang , Senior Member, IEEE, Zhuoyue Cao, Deliang Xiang , Canbin Hu, Fei Ma ,  
Qiang Yin , Member, IEEE, and Yongsheng Zhou , Member, IEEE

**Abstract**—Compact polarimetry (CP) has attracted much attention in recent years due to its hybrid dual-polarization imaging mode. CP synthetic aperture radar has a larger swath and can provide more polarimetric information compared with the traditional dual-polarization imaging mode (HH/HV or VH/VV). Pseudo quad-polarimetric (quad-pol) data reconstruction is an important technology in the application of CP data. The goal of pseudo quad-pol data reconstruction from CP data is to change the form of CP data to the form of quad-pol data without increasing any new information. In this article, a new pseudo quad-pol data reconstruction method from the CP data is proposed. This method combines a complex-valued dual-branch convolutional neural network (CV-DBCNN) to achieve the reconstruction of the pseudo quad-pol data. It utilizes complex-valued convolutional layers and a complex-valued activation function to fully extract the polarimetric information embedded in the complex-valued CP data. For the CV-DBCNN, the branch with  $1 \times 1$  kernel size is used to nonlinearly and self-adaptively combine the channel of input data, and the branch with  $3 \times 3$  kernel size is used to extract the discriminative regional polarimetric features. Furthermore, polarimetric decomposition is utilized to evaluate the scattering mechanisms of the pseudo quad-pol data. Three state-of-the-art methods are utilized for comparison. In comparison with other methods, our proposed reconstruction method based on the CV-DBCNN shows its superiority in terms of the pseudo quad-pol data reconstruction and scattering mechanism preservation.

**Index Terms**—Compact polarimetry (CP), complex-valued dual-branch convolutional neural network (CV-DBCNN), deep learning, pseudo quad-polarization (quad-pol) data reconstruction, synthetic aperture radar (SAR).

Manuscript received July 22, 2021; revised September 2, 2021 and November 27, 2021; accepted December 17, 2021. Date of publication December 31, 2021; date of current version January 13, 2022. This work was supported in part by the National Natural Science Foundation of China under Grants 61871413, 61801015, and 41801236 and in part by the Fundamental Research Funds for the Central Universities under Grant buctrc202121. (Corresponding author: Deliang Xiang.)

Fan Zhang is with the College of Information Science and Technology and the Interdisciplinary Research Center for Artificial Intelligence, Beijing University of Chemical Technology, Beijing 100029, China (e-mail: zhangf@mail.buct.edu.cn).

Zhuoyue Cao, Canbin Hu, Fei Ma, Qiang Yin, and Yongsheng Zhou are with the College of Information Science and Technology, Beijing University of Chemical Technology, Beijing 100029, China (e-mail: 2019200797@mail.buct.edu.cn; canbinhu@163.com; mafef@mail.buct.edu.cn; yinq@mail.buct.edu.cn; zhyosh@mail.buct.edu.cn).

Deliang Xiang is with the Beijing Advanced Innovation Center for Soft Matter Science and Engineering and the Interdisciplinary Research Center for Artificial Intelligence, Beijing University of Chemical Technology, Beijing 100029, China (e-mail: xiangdeliang@gmail.com).

Digital Object Identifier 10.1109/JSTARS.2021.3138781

## I. INTRODUCTION

AS ONE kind of imaging radar technology, synthetic aperture radar (SAR) can obtain the land-cover images under all-time and all-weather conditions. Among them, quad-polarimetric (quad-pol) SAR provides multichannel polarimetric information, which can extract the polarimetric features of different land covers [1]. In 2005, a concept of polarimetric imaging, commonly known as compact polarimetry (CP), was proposed [2]. The quad-pol system needs to alternately transmit horizontal (H) and vertical (V) linearly polarizations, while CP only needs to transmit one polarization. Both systems receive backscatter in two orthogonal polarizations.

Compared with the quad-pol system, the CP system has lower system complexity, so that it has larger swath coverage with fewer downloading data and lower budget requirements. Compared with the traditional dual-polarization (dual-pol) system, the CP system can store the phase of echo signal, leading to a more flexible signal combination. Therefore, it can obtain more comprehensive polarimetric information [3], [4]. In addition, the CP system has the advantages of providing large imaging strip compared with the dual-pol system, which has great potential in large-scale region monitoring.

Until now, three CP modes have been proposed, namely the  $\pi/4$  mode, the dual circular polarimetric (DCP) mode, and the hybrid polarimetric (HP) mode. The  $\pi/4$  mode transmits  $45^\circ$  linear polarization and receives H and V linear polarizations [2]. The DCP mode transmits left-handed or right-handed circularly polarization and receives left-handed and right-handed circularly polarizations [5]. The HP mode, which transmits left-handed or right-handed circularly polarization and receives H and V linear polarizations, is also called the circular transmit and linear receive [3]. CP SAR has achieved remarkable achievements in some applications [6]–[11]. Ohki and Shimada [12] used quad-pol, CP, and dual-pol data for land-use and land-cover classification. The results indicate that the CP SAR and the dual-pol SAR have the advantages of large-scale coverage and compact data volume. Nevertheless, the classification performance is slightly worse than that of the quad-pol SAR. Shirvany *et al.* [13] proposed a classification technique based on a neural network for CP data with the HP mode and explored the potential of real CP data for the sea ice classification. Yang *et al.* [14] extracted 149-D features from time-series optical data, quad-pol data, and

simulated CP data and then used a multiclass correlation vector machine to implement the phenological phase classification of the transplanted indica rice field and direct-sown japonica rice field. Nunziata *et al.* [15] evaluated the ability of CP data with the HP mode in distinguishing oil slicks from weak-damping look-alikes and proved that CP SAR data with the HP mode have remarkable performance in this task.

The processing method of CP data can be divided into two categories. One is directly extracting the information of CP data to describe the polarimetric scattering characteristics of objects [16]–[19]. Charbonneau *et al.* [16] proposed a three-component decomposition method for CP data, namely,  $m$ - $\delta$  decomposition, and further evaluated the potential of the CP system for operational use. Raney *et al.* [17] proposed  $m$ - $\chi$  decomposition to describe the double-bounce scattering effect of craters on the lunar surface. However, both  $m$ - $\delta$  decomposition and  $m$ - $\chi$  decomposition have the disadvantage on overestimation of volume scattering. Han *et al.* [18] applied the Freeman–Durden decomposition method [19] to the CP data, but the problem of volume scattering overestimation still exists. Another one is to simulate the coherence matrix or the covariance matrix of quad-pol data from the CP data, i.e., reconstruct the pseudo quad-pol data with some assumptions. In this article, we also regard the simulation as reconstruction. In this way, we can directly apply the traditional quad-pol data processing and application algorithms to the CP data. Therefore, quad-pol data reconstruction from CP data is a prospective research direction. However, there still exist some challenges in this research field.

In the quad-pol data reconstruction, the common difficulty is that CP SAR only measures two channels of information, whereas quad-pol SAR measures four channels of information. Although we can turn the quad-pol data into three channels by assuming scattering reciprocity, the expansion from the  $2 \times 2$  CP covariance matrix to the  $3 \times 3$  pseudo quad-pol covariance matrix still requires extra assumptions. In 2005, Souyris *et al.* [2] first proposed the CP concept of the  $\pi/4$  mode and designed the reconstruction model with a constant  $N$ , which means the relationship between the ratio of the cross-pol intensity to the mean of the co-pol intensity and the copolarized coherence. This method is suitable for the areas dominated by volume scattering, but not suitable for regions dominated by surface or double-bounce scattering. Nord *et al.* [20] found that the Souyris's method oversimplified the complexity of natural media by simply setting the value of  $N$  as 4 and proposed a reconstruction method, where the relationship between co-pol coherence and the ratio of cross-pol intensity to the mean of the co-pol intensity is corrected based on the statistics. However, the relationship may not be fine in some areas, such as the sea surface and sea ice areas [21]–[23]. The parameter  $N$  is generated after several iterations, which will increase the computational complexity. Therefore, many scholars have proposed a series of pseudo quad-pol reconstruction methods for various applications in different specific regions. Collins *et al.* [21] improved the Nord's method and proposed a reconstruction method for ocean scenes, which can be used to detect ships and icebergs in the ocean. Li *et al.* [22] proposed a reconstruction method for oil spill detection on sea surface. Espeseth *et al.* [23]

proposed two reconstruction methods for sea ice with  $C$ - and  $L$ -band SAR, respectively. However, for the reason that some assumptions are only approximately effective in some specific cases, these methods can only achieve ideal results in some specific areas. Yue *et al.* [24] developed a Wishart–Bayesian optimization model based on the complex Wishart distribution of the quad-pol covariance matrix. However, the reconstruction effect heavily depends on the prior knowledge obtained by averaging the quad-pol images of the target region, which is difficult to achieve in practical applications. Yin *et al.* [25] proposed a reconstruction method based on the three-component decomposition [19], [26]. The cross-polarization term is solved by an iterative method. Based on the reconstruction method of [25], Yin *et al.* [27] further proposed the least-squares (LS) estimator to more accurately reconstruct quad-pol data from CP data, but it requires a local minimum for each pixel, resulting in more computation cost than the iterative algorithm. Besides, the LS estimator reduces the resolution of CP data due to the local window averaging, and the high cost of time and computing also limit the application of the LS estimator. In recent years, deep learning algorithms represented by the convolution neural networks (CNNs) have achieved great success in the field of SAR image processing, such as image classification [28]–[30], target detection [31]–[34], and image segmentation [35]–[37]. Research on the application of deep learning algorithms in quad-pol data reconstruction is ongoing. Song *et al.* [38] proposed a quad-pol data reconstruction method based on a pretrained neural network from single-pol images. Gu *et al.* [39] proposed a fully convolutional network named the quad-pol reconstruction fully convolutional network (QPRFCN) to reconstruct quad-pol data from CP data and improved the reconstruction effect compared with other traditional methods. The biggest advantage of using the deep neural network for the pseudo quad-pol data reconstruction is that the pseudo quad-pol data can be directly reconstructed from CP data with the neural network without introducing any artificial assumptions [2], [25], [27]. However, the polarimetric features embedded in the CP data could not be fully extracted, and the accuracy and generalization ability of QPRFCN in pseudo quad-pol data reconstruction needs to be further improved.

The phase information of SAR data is very important. For quad-pol data, the phase information of the off-diagonal terms of the covariance or coherence matrix is useful in distinguishing different types of scatterers. Therefore, it is necessary to develop a complex version of the convolutional neural network to fully extract the polarimetric information of the complex-valued quad-pol data. Hirose [40] first applied the complex-valued convolutional neural network (CV-CNN) to the land-surface classification [40]. Zhang *et al.* [41] applied the CV-CNN to the quad-pol SAR image classification task.

Similar to the quad-pol data, the CP data also have phase information. For the traditional CP data reconstruction methods [2], [25], [27], the phase information of the off-diagonal term of the CP covariance matrix is indispensable. However, the CV-CNN has not been used to reconstruct pseudo quad-pol data from CP data. Therefore, in this study, we propose a complex-valued dual-branch convolutional neural network (CV-DBCNN) for

pseudo quad-pol data reconstruction from CP data. In particular, we use a branch with  $1 \times 1$  kernel size to nonlinearly combine the channels from the input data, resulting in nonlinear combination relationships of the channels from the input CP data. Furthermore, we use a branch with  $3 \times 3$  kernel size to extract the discriminative regional polarimetric features. With the combination of the branch with  $1 \times 1$  kernel size and the branch with  $3 \times 3$  kernel size, we can find the mapping relationship between the CP data and the pseudo quad-pol data. Moreover, we verify the functions of the two branches of the CV-DBCNN by comparing the reconstruction effect of a single-branch network with the  $3 \times 3$  kernel size convolutional network and the proposed CV-DBCNN. Note that during the reconstruction process, we only change the form of the CP data to the form of quad-pol data without increasing any new polarimetric information, which can make the CP data be directly processed with the existing approaches designed for the quad-pol data. Three state-of-the-art methods are utilized for comparison. The QPRFCN and the LS estimator are two selected methods. In addition, the degree of polarization (DoP) method proposed by Espeseth *et al.* [23] is also utilized in the experiment. Experiments on three CP datasets with different sensors demonstrate the effectiveness of the proposed method. The main contributions of this article are shown as follows.

- 1) A novel pseudo quad-pol simulation method from CP data based on a CV-DBCNN is proposed.
- 2) The complex-valued convolution and the complex-valued activation function are used to fully extract the polarimetric features for the first time. Three state-of-the-art methods are conducted for comparison on three quad-pol images acquired by different sensors.

The rest of this article is organized as follows. Section II introduces the network structure of our proposed method. The descriptions of the datasets are given in Section III. Section IV shows experimental results and comparisons. Finally, Section V concludes this article.

## II. METHODOLOGY

This section gives the information of the inputs for the reconstruction of pseudo quad-pol data. Then, the structure of our proposed CV-DBCNN is discussed, followed by the analysis of its advantages.

### A. Preparation of the Input Data

The goal of pseudo quad-pol data reconstruction from CP data is to estimate a pseudo quad-pol covariance matrix  $C_{\text{pseudo}}$  from a CP covariance matrix with the  $\pi/4$  mode  $C_{\text{cp}}$ . Until now, the ALOS-2, Canadian RCM [42], RISAT-1, and SAOCOM SAR satellites have been equipped with CP SAR imaging systems. In specific, the ALOS-2 satellite is equipped with several acquisition modes, such as dual-pol, quad-pol, and CP, for experimental purpose, and the data of the RCM satellite are not open source. In addition, no satellite system operates in the  $\pi/4$  mode for earth observation purpose. Therefore, the  $\pi/4$  mode CP data used in this article can only be simulated from the quad-pol data.

The polarimetric covariance matrices for the real quad-pol data and the  $\pi/4$  mode CP data are given by (1) and (2), respectively:

$$C_{\text{qp-real}} = \begin{bmatrix} \langle |S_{\text{hh}}|^2 \rangle & \sqrt{2} \langle S_{\text{hh}} S_{\text{hv}}^* \rangle & \langle S_{\text{hh}} S_{\text{vv}}^* \rangle \\ \sqrt{2} \langle S_{\text{hv}} S_{\text{hh}}^* \rangle & 2 \langle |S_{\text{hv}}|^2 \rangle & \sqrt{2} \langle S_{\text{hv}} S_{\text{vv}}^* \rangle \\ \langle S_{\text{vv}} S_{\text{hh}}^* \rangle & \sqrt{2} \langle S_{\text{vv}} S_{\text{hv}}^* \rangle & \langle |S_{\text{vv}}|^2 \rangle \end{bmatrix} \quad (1)$$

$$C_{\text{cp}} = \begin{bmatrix} J_{11} & J_{12} \\ J_{12}^* & J_{22} \end{bmatrix} \\ = \frac{1}{2} \left\{ \begin{bmatrix} \langle |S_{\text{hh}}|^2 \rangle & \langle S_{\text{hh}} S_{\text{vv}}^* \rangle \\ \langle S_{\text{vv}} S_{\text{hh}}^* \rangle & \langle |S_{\text{vv}}|^2 \rangle \end{bmatrix} + \langle |S_{\text{hv}}|^2 \rangle \begin{bmatrix} 1 & 1 \\ 1 & 1 \end{bmatrix} \right. \\ \left. + \begin{bmatrix} 2\text{Re} \langle S_{\text{hh}} S_{\text{hv}}^* \rangle & \langle S_{\text{hh}} S_{\text{hv}}^* \rangle + \langle S_{\text{hv}} S_{\text{vv}}^* \rangle \\ \langle S_{\text{hv}} S_{\text{hh}}^* \rangle + \langle S_{\text{vv}} S_{\text{hv}}^* \rangle & 2\text{Re} \langle S_{\text{vv}} S_{\text{hv}}^* \rangle \end{bmatrix} \right\} \quad (2)$$

where  $S$  is the complex backscattering element. The subscript  $hv$  demotes the horizontal polarization  $h$  in reception and vertical polarization  $v$  in transmission. The variables  $J$  are the elements of the  $2 \times 2$  CP covariance matrix with the  $\pi/4$  mode.  $\langle \cdot \rangle$  denotes the ensemble averaging and superscript  $*$  denotes complex conjugation. The real and imaginary parts of a complex number  $z$  are denoted by  $\text{Re}(z)$  and  $\text{Im}(z)$ , respectively.

$$C_{\text{pseudo}} = \begin{bmatrix} 2 \langle J_{11} \rangle - \langle |S_{\text{hv}}|^2 \rangle_c & 0 & 2 \langle J_{12} \rangle - \langle |S_{\text{hv}}|^2 \rangle_c \\ 0 & 2 \langle |S_{\text{hv}}|^2 \rangle_c & 0 \\ 2 \langle J_{12}^* \rangle - \langle |S_{\text{hv}}|^2 \rangle_c & 0 & 2 \langle J_{22} \rangle - \langle |S_{\text{hv}}|^2 \rangle_c \end{bmatrix}. \quad (3)$$

According to (1) and (2), we can simulate CP data from the real quad-pol data [2], [24], [39]. Note that the window size used here is set as  $3 \times 3$ , which is commonly used as the calculation of the sample polarimetric covariance/coherency matrix. A larger window size would decrease the simulated CP data resolution. In this article, we focus on the pseudo quad-pol data reconstruction from the simulated CP data and then evaluate the performance in comparison with the real quad-pol data. It should be noted that during the reconstruction, we only change the form of the CP data to the form of quad-pol data, which is beneficial to the CP data interpretation with the existing algorithms designed for quad-pol data. However, it is impossible to reconstruct the complete quad-pol information from the CP data without introducing any new polarimetric information. From (1) and (2), it can be seen that the cross-polarized term  $\langle |S_{\text{HV}}|^2 \rangle$  is the most important and difficult part to be reconstructed because of the weaker intensity of the return signal and the lower signal-to-noise ratio of the cross-polarized term than the other terms [39]. After reconstructing the cross-polarization channel, we still cannot reconstruct the full quad-pol covariance matrix because the knowns are fewer than the unknowns. Therefore, we introduce a constraint to reduce the difficulty of reconstruction and the uncertainty in the reconstruction process.

The reflection symmetry is generally used in the equation solution of polarimetric decomposition, which can simplify the



polarimetric covariance matrix [2], [39]. The reflection symmetry is shown as

$$\langle S_{hh}S_{hv}^* \rangle \approx \langle S_{vv}S_{hv}^* \rangle \approx 0. \quad (4)$$

With the reflection symmetry, we can simplify the real quad-pol covariance matrix and then derive the polarimetric covariance matrix of pseudo quad-pol data as (3), where  $\langle |S_{HV}|^2 \rangle_c$  represents the reconstructed cross-polarized term. It can be seen that after the reconstruction of the cross-polarized term, we can simply reconstruct the pseudo quad-pol polarimetric covariance matrix by some linear additions, which is consistent with the previously proposed methods [2], [25], [27], [39]. As the quad-pol data has more polarimetric information than the CP data, new information must be introduced to achieve the reconstruction from CP data to quad-pol data. However, our object is to change the form of CP data to the form of quad-pol data without increasing any new information; therefore, we must introduce reflection symmetry to achieve our goal, for which the reflection symmetry will be the key to complement the information. Thus, the method proposed in this article is suitable for the areas satisfying reflection symmetry.

The polarimetric covariance matrix elements of CP data are utilized to generate the input to our proposed reconstruction network. We expand the covariance matrix of each pixel of the input CP data to a 4-D input vector, which can be defined as

$$\mathbf{T}_{4-D} = [J_{11}, J_{22}, \text{Mod}(J_{12}), J_{12}]^T. \quad (5)$$

On the basis of (2), the 4-D input vector can also be rewritten as

$$\mathbf{T}_{4-D} = \frac{1}{2} \begin{bmatrix} \langle |S_{hh}|^2 \rangle + \langle |S_{hv}|^2 \rangle + 2 \text{Re} \langle S_{hh}S_{hv}^* \rangle \\ \langle |S_{vv}|^2 \rangle + \langle |S_{hv}|^2 \rangle + 2 \text{Re} \langle S_{vv}S_{hv}^* \rangle \\ \text{Mod} \left( \langle S_{hh}S_{vv}^* \rangle + \langle |S_{hv}|^2 \rangle + \langle S_{hh}S_{hv}^* \rangle + \langle S_{hv}S_{vv}^* \rangle \right) \\ \langle S_{hh}S_{vv}^* \rangle + \langle |S_{hv}|^2 \rangle + \langle S_{hh}S_{hv}^* \rangle + \langle S_{hv}S_{vv}^* \rangle \end{bmatrix}. \quad (6)$$

It can be observed that the elements of the input vector and the elements in the CP covariance matrix are one-to-one mappings. Considering that the module of  $J_{12}$  is often used to generate intermediate features in experience-based reconstruction methods, the module of  $J_{12}$  is put in the input vector as an isolated channel. Fig. 1 shows the generation of the input vector for the pseudo quad-pol data construction.

### B. Complex-Valued Dual-Branch Convolutional Neural Network

To reconstruct the pseudo quad-pol data from CP data, we propose a CV-DBCNN in this article. Since  $J_{12}$  is complex, we use the complex convolutional layers and the complex activation function to make the neural network extract the amplitude and phase information of  $J_{12}$ . The complex convolutional is calculated as [41]

$$O_i^{(l+1)} = f \left( \Re \left( V_i^{(l+1)} \right) \right) + j f \left( \Im \left( V_i^{(l+1)} \right) \right) \quad (7)$$

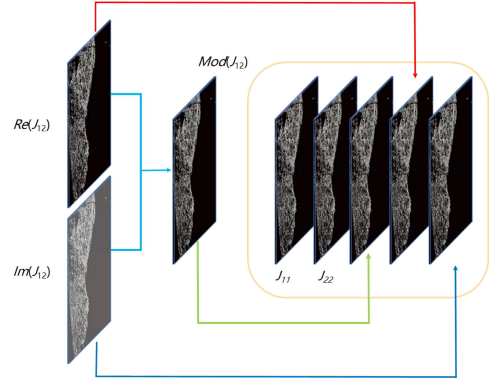


Fig. 1. 4-D input data for the pseudo quad-pol data construction.

$$\begin{aligned} V_i^{(l+1)} &= \sum_{k=1}^K w_{ik}^{(l+1)} * O_k^{(l)} + b_i^{(l+1)} \\ &= \sum_{k=1}^K \left( \Re \left( w_{ik}^{(l+1)} \right) \Re \left( O_k^{(l)} \right) - \Im \left( w_{ik}^{(l+1)} \right) \cdot \Im \left( O_k^{(l)} \right) \right) \\ &\quad + j \sum_{k=1}^K \left( \Re \left( w_{ik}^{(l+1)} \right) \cdot \Im \left( O_k^{(l)} \right) \right. \\ &\quad \left. + \Im \left( w_{ik}^{(l+1)} \right) \cdot \Re \left( O_k^{(l)} \right) \right) + b_i^{(l+1)} \end{aligned} \quad (8)$$

where character  $*$  represents the convolution operation, and  $\Re$  and  $\Im$  represent the real part and the imaginary part of a complex number, respectively.  $O_k^{(l)}$  means the  $k$ th output feature map of the  $l$ th layer.  $V_i^{(l+1)}$  represents the  $i$ th output feature map of the  $(l+1)$ th convolutional layer.  $f(\cdot)$  means the activation function. The complex-valued activation function used in this article is defined as

$$f(z) = \text{LeakyReLU}(\Re(z)) + i \text{LeakyReLU}(\Im(z)). \quad (9)$$

When performing complex-valued convolution, both the real and imaginary parts of the complex data are input into one complex-valued convolutional layer together. In order to keep the form of the elements in the 4-D input vector consistent, we change the real number elements to a complex number form, by keeping the real part unchanged and setting the imaginary part to zero. With the complex value convolutional layers and the complex value activation function, the CV-DBCNN can extract complex polarimetric information. In contrast, the QPRFCN proposed by Gu *et al.* [39] utilized real-valued convolutional layers and the activation function, which cannot maintain the phase information of the CP complex data.

Fig. 2 gives the architecture of our proposed network. Specifically, the CV-DBCNN contains eight  $3 \times 3$  convolutional layers and three  $1 \times 1$  convolutional layers with the activation function and the last one convolutional layer without the activation function. There are two branches within the network. The first branch with  $3 \times 3$  kernel size, namely, the regional polarimetric



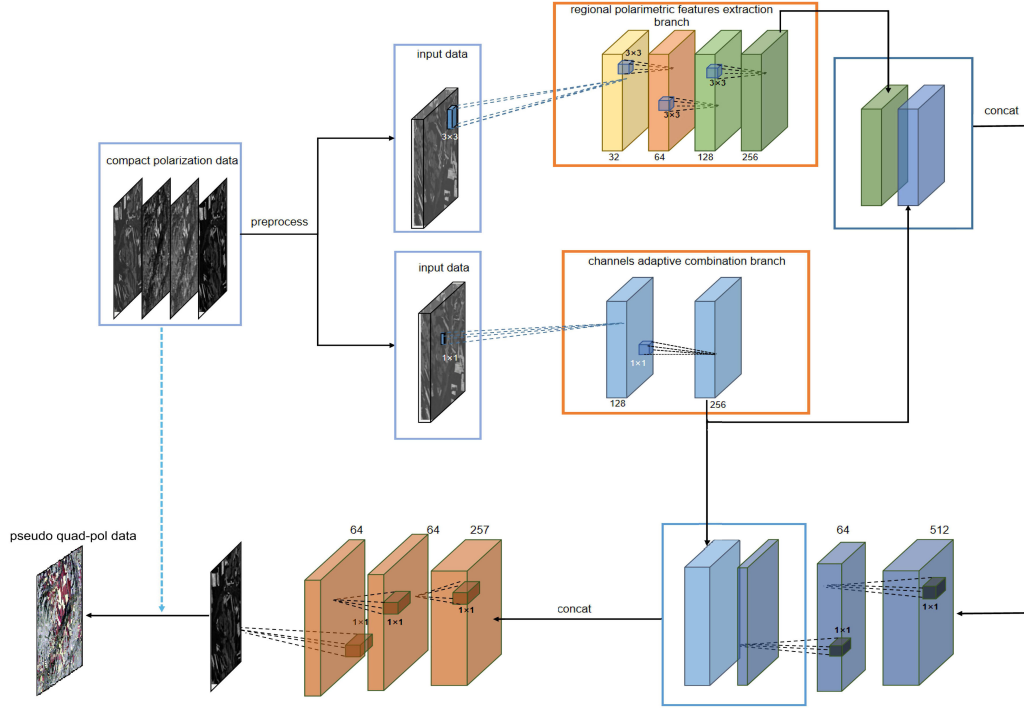


Fig. 2. Network structure for pseudo quad-pol data reconstruction from CP data.

feature extraction branch, is composed of cascaded four  $3 \times 3$  convolutional layers, which are used to extract discriminative regional polarimetric features. The other branch with  $1 \times 1$  kernel size, namely, the self-adaptive channel combination branch, is used to nonlinearly and self-adaptively combine the channels of the input data. Thanks to the utilization of  $1 \times 1$  convolutional branch, the CV-DBCNN is more lightweight than the QPRFCN. A lightweight network is easier to converge and can effectively prevent overfitting with limited training data [43].

Because the QPRFCN [39] does not consider the retention of phase information and the adaptive combination between channels of the input data, its network generalization performance is limited. The QPRFCN directly stacks and shortcuts multiple  $3 \times 3$  convolution layers, which leads to a larger receptive field. Thus, it will make one pixel in the reconstructed data to be influenced by its surrounding area, resulting in the reconstruction result deviating from the real quad-pol data seriously. Experimental results in Sections IV and V confirm that the reconstruction effect of the QPRFCN seriously deviates from the real quad-pol data, and the Pauli-basis images reconstructed by the QPRFCN shows discontinuities between adjacent blocks. Due to the limited video memory size of the equipment we use, we have to split the original image into multiple small patches ( $512 \times 512$ ) for reconstruction and then stitch them into a whole image. When the block size is small, the reconstruction results of the QPRFCN have serious discontinuities between adjacent blocks, indicating that the reconstruction results of the QPRFCN are very unstable.

The CV-DBCNN uses a  $1 \times 1$  branch, which increases the number of learnable parameters in the network without increasing the receptive field. Obviously, this strategy helps to

obtain more accurate reconstruction results. By combining the branch with  $3 \times 3$  kernel size and the branch with  $1 \times 1$  kernel size together, the dual-branch convolutional network will learn the regional polarimetric features of the training data. In the meantime, the nonlinear combination relationships between the channels of the input CP data will be generated. To make a further evaluation, we remove the branch with  $1 \times 1$  kernel size in the CV-DBCNN and compare the reconstruction effect of this single-branch convolutional network with that of the original CV-DBCNN. This is to verify whether combining the branch with  $3 \times 3$  kernel size and the branch with  $1 \times 1$  kernel size together could achieve better reconstruction results than the network with only a branch with  $3 \times 3$  kernel size. The training data and the training strategies of the two networks are the same. The detailed comparisons are shown in Section IV.

### C. Loss Function

Because the pseudo quad-pol data reconstruction from CP data is a regression problem, the mean absolute error (MSE) between the real quad-pol data and the output of the network can be used as the loss function.

The loss function is given by

$$L = \text{MSE}(\theta) = \frac{1}{WH} \sum_{W=0}^{W-1} \sum_{h=0}^{H-1} (T_{\theta}(I) - Y)^2 \quad (10)$$

where  $\theta$  represents the weights of the proposed neuron network.  $Y$  is the real quad-pol covariance matrix term.  $T_{\theta}(I)$  is the output of the reconstructed network and  $I$  is the input data of the network.  $W$  and  $H$  denote the 2-D spatial index. The

---

**Algorithm 1:** Quad-Pol Data Reconstruction Algorithm of the CV-DBCNN.

---

**Input:**  $J_{11}J_{12}J_{22}$ 
**Output:** Reconstructed quad-pol data  $C_{\text{pseudo}}$ 

- 1: Calculate the  $Mod(J_{12})$  and generate the 4-D input vector.
  - 2: Change the  $J_{11}J_{22}$  and  $Mod(J_{12})$  into the plural form.
  - 3: Feed the input data into the CV-DBCNN.
  - 4: Obtain the reconstructed cross-polarized term  $\langle |S_{HV}|^2 \rangle_c$  with the proposed network.
  - 5: According to (3), reconstruct the pseudo covariance matrix  $C_{\text{pseudo}}$ .
  - 6: **return** the  $C_{\text{pseudo}}$
- 

TABLE I  
INFORMATION OF THE QUAD-POL DATASETS

Sensor	Region	Resolution	Size	Band
GF-3	Hulunbeier Grassland	3m	3267×3580	C
ESAR	Munich	3m	1295×1896	L
UAVSAR	Kumamoto	5m	1297×2478	L

Adam optimization algorithm is used to update the weights of the network.

It is worth pointing out that the CV-DBCNN learns the reconstruction process from the CP data to pseudo quad-pol data without increasing any new polarimetric information. Therefore, it is impossible to reconstruct the complete full polarization information from the CP data for the reason that it does not conform to the principle of energy conservation. As we stated before, the main work of our proposed method is how to convert the CP data form into the quad-pol data form with some certain assumptions. Since the reconstructing of quad-pol data from CP data is essentially an ill-posed problem, there is no definite and unique solution for the pseudo quad-pol reconstruction. However, in comparison with the state-of-the-art methods, our proposed method can achieve the best results in all indicators, which is closer to the real quad-pol data. Algorithm 1 gives the brief pseudo quad-pol data reconstruction procedure.

### III. DESCRIPTION OF THE EXPERIMENTAL DATASETS

All the data used in this article are the simulated CP data with the  $\pi/4$  mode from quad-pol data. We choose three quad-pol datasets, and the corresponding information is listed in Table I. The dataset from the Hulunbeier Grassland region is acquired by the GF-3 C-band sensor. The size is 3267×3580 and the resolution is about 3 m. This image consists of three land-cover types, namely, mountains, forests, and agriculture areas. The dataset from Munich region (ESAR) is an L-band dataset, for which the size is 1295×1896 and the resolution is about 3 m. These data consist of two land-cover types, including agriculture and urban areas. The dataset from the Kumamoto region is the L-band UAVSAR dataset. The image size is 1325×2478 and the

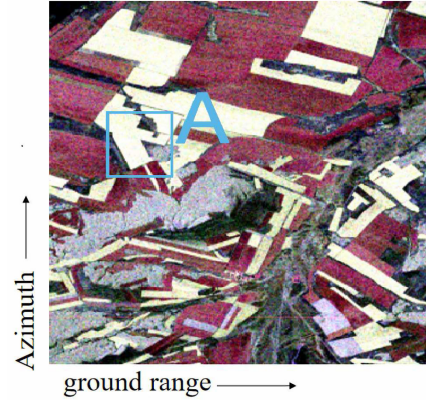


Fig. 3. Pauli-basis image of GF-3 quad-pol data, Hulunbeier Grassland region. Area A belongs to the agriculture area. The red, green, and blue channels of the Pauli-basis image represent the double-bounce scattering, volume scattering, and single-bounce scattering of quad-pol data, respectively.

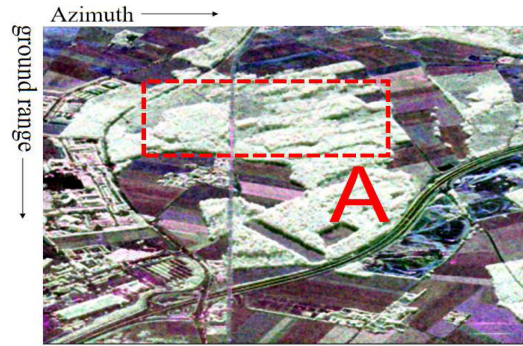


Fig. 4. Pauli-basis image of ESAR data, Munich region. Area A belongs to forest area. The red, green, and blue channels of the Pauli-basis image represent the double-bounce scattering, volume scattering, and single-bounce scattering of quad-pol data, respectively.

resolution is about 5 m. The UAVSAR data consist of three land-cover types, namely, water bodies, agriculture, and urban areas. Details of the training and testing datasets are listed in Table II. It can be seen that we use 2.13% of the UAVSAR data for network training; 97.87% of the image is used for testing. The size of the testing UAVSAR image is 1297×2478. To demonstrate the generality of the proposed method, the whole GF-3 and ESAR datasets are used for testing.

Figs. 3–5 depict the Pauli-basis images of three real quad-pol datasets. We select three different regions from the testing data, which belong to three different terrain types, namely, the water body, the forest, and the farm land, to analyze the reconstruction results. The Pauli-basis image of the original quad-pol GF-3 data is shown in Fig. 3. Area A belongs to agriculture area. The Pauli-basis image of the original quad-pol ESAR testing data is shown in Fig. 4, in which area A belongs to forest area. The Pauli-basis image of the original real quad-pol UAVSAR data is shown in Fig. 5, in which area A belongs to water area.

TABLE II  
PROPORTIONS OF DATASETS USED FOR TRAINING AND TESTING

Data	Training (number of pixels)	Testing (number of pixels)	Training (proportion)	Testing (proportion)
UAVSAR (Kumamoto)	69968	3213966	2.13%	97.87%
ESAR (Munich)	0.00	2455320	0.00%	100%
GF-3 (Hulunbeier Grassland)	0.00	11695860	0.00%	100%

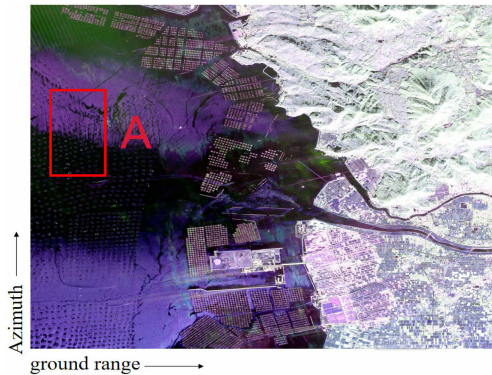


Fig. 5. Pauli-basis image of UAVSAR quad-pol data, Kumamoto region. Area A belongs to the water area. The red, green, and blue channels of the Pauli-basis image represent the double-bounce scattering, volume scattering, and single-bounce scattering of quad-pol data, respectively.

#### IV. EXPERIMENTAL RESULTS AND ANALYSIS

##### A. Parameter Settings

In the CV-DBCNN, the weights of the convolutional filters are initialized by the Kaiming initialization. The proposed network uses a 12-layer convolutional structure, in which the previous 11 layers are the convolutional layers with the activation function and the last layer is a convolutional layer. The learning rate is initialized to 0.001 for the whole network, which is fixed. In the network training stage, the maximum number of iterations is set to 1000. The Adam algorithm is used for weight optimization of the network. We use the PyTorch framework to train the proposed method with the Windows 10 environment, 16-GB RAM, a NVIDIA GeForce RTX 2070 GPU, and Intel CORE i5-8500 CPU.

##### B. Quantitative Error Indicators

In order to quantitatively compare the reconstruction performance of the LS estimator [27], the QPRFCN [39], and our proposed CV-DBCNN, we introduce a series of evaluation indicators.

The MAE is introduced as a quantitative evaluation indicator, which is used to measure the absolute error between the reconstructed cross-polarized term and the real cross-polarized term of the quad-pol polarimetric covariance matrix. The smaller the MAE, the better the reconstruction performance. Because the values of the MAE are related to the numerical range of the cross-polarized term, we normalize the cross-polarized term to [0–1] for error analysis. In addition, we introduce the coherence index (COI) as a quantitative indicator to measure the similarity between the reconstructed cross-polarized term and the real

cross-polarized term, as follows:

$$\text{COI}(A, B) = \frac{\sum_{i=1}^m (a_i b_i)}{\sqrt{\sum_{i=1}^m (a_i a_i) \cdot \sum_{i=1}^m (b_i b_i)}} \quad (11)$$

where  $A = [a_1, a_2, \dots, a_m]$  represents the results of real cross-polarized term,  $B = [b_1, b_2, \dots, b_m]$  represents the results of reconstructed cross-polarized term, and  $m$  is the total number of pixels. The value range of the COI is [0, 1]. The larger the COI, the better the reconstruction performance.

##### C. Comparison Between the Single-Branch Network and the CV-DBCNN

The advantage of combining the branch with  $3 \times 3$  kernel size and the branch with  $1 \times 1$  kernel size together is fully discussed in Section II-B. To demonstrate this issue, we conduct an experiment to compare the reconstruction results of the CV-DBCNN and a single-branch with  $3 \times 3$  kernel size convolutional network. Fig. 6 gives the reconstructed Pauli-basis images of the ESAR data with the single-branch network and CV-DBCNN approach. As shown in Fig. 6(b) and (c), the reconstruction result of the single-branch with the  $3 \times 3$  kernel size convolutional network shows an obvious overestimation of the volume scattering, as well as a lot of noise generated in the forest area. In contrast, the result of the CV-DBCNN is more closer to the original quad-pol data. The reason is that the CV-DBCNN can extract the regional polarimetric features and the nonlinear combination relationships between the channels of the input CP data, whereas the single-branch network can only extract the regional polarimetric features. Therefore, the CV-DBCNN can preserve more precise polarimetric information than the single-branch network.

##### D. Comparison Results on Different Terrain Types With Different Methods

In this subsection, three state-of-the-art methods are introduced for comparison, which are the QPRFCN proposed in [39], the LS estimator proposed in [27], and the DoP method proposed by Espeseth *et al.* [23]. We compare the reconstruction performance of CV-DBCNN, QPRFCN, LS, and DoP-based estimator on the GF-3 data, UAVSAR data, and ESAR data, respectively. We introduce scatter spots to evaluate the reconstruction performance of the cross-polarized term (i.e.,  $\langle |S_{hv}|^2 \rangle$ ), which are presented in the logarithm domain.

First of all, we compare the pseudo quad-pol data reconstruction results of the LS estimator, the QPRFCN, the DoP-based method, and the CV-DBCNN on UAVSAR data (Kumamoto region). As shown in Fig. 7(a) and (b), for the water area of UAVSAR data, the LS estimator and the QPRFCN both show obvious overestimation error of the cross-polarized term.



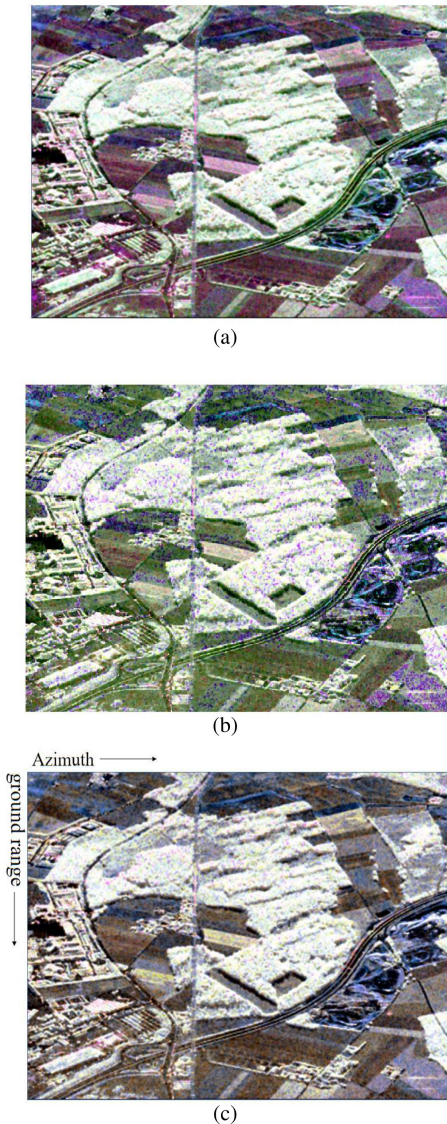


Fig. 6. Pauli-basis images of the real quad-pol data and the reconstructed pseudo quad-pol data (ESAR). (a) Real quad-pol data. (b) Result of the single-branch network. (c) Result of the CV-DBCNN. The red, green, and blue channels of the Pauli-basis image represent the double-bounce scattering, volume scattering, and single-bounce scattering, respectively.

The scatter spot distribution of the LS estimator is obviously discontinuous, especially for the pixels with lower backscattering intensities. This is because the LS estimator estimates the cross-polarized term of each pixel in a set interval. However, the scatter spot distribution of the CV-DBCNN is continuous. In Fig. 8(b) and (c), we can see that the LS estimator overestimates the double-bounce scattering, which makes the water area look red. The QPRFCN overestimates the volume scattering, which makes the water area looks green. The DoP-based method is designed based on an assumption that the cross-polarized scattering is fully contributed by the depolarized wave, making the DoP-based method suitable for the area such as sea ice [23]. Since the scattering features of water area are similar to those of the sea ice, the result of the DoP-based method is closer to the real quad-pol data than that of the LS estimator and the

QPRFCN. Fig. 8(e) shows that the Pauli-basis simulation result of the DoP-based method is close to the real data, whereas the cross-polarized term is seriously overestimated, as shown in Fig. 7(c). As shown in Figs. 7(d) and 8(e), the CV-DBCNN can achieve satisfactory reconstruction performance for the water area, which indicates that the CV-DBCNN has better generalization performance than other methods.

Second, we compare the pseudo quad-pol data reconstruction effect of the LS estimator, the QPRFCN, the DoP-based method, and the CV-DBCNN on forest area (area A) in ESAR data (Munich region). For the forest area, the LS estimator, the QPRFCN, and the DoP-based method underestimate the cross-polarized term, as shown in Fig. 9. We can obviously see that in Fig. 10(b), the LS estimator overestimates the single-bounce scattering of the forest area. In Fig. 10(c), the QPRFCN overestimates the single-bounce scattering. The QPRFCN consists of 11 cascaded  $3 \times 3$  convolutional layers. The deeper the layer, the larger the networks perception field. However, in the reconstruction of pseudo quad-pol data, a too large receptive field will lead to inaccurate predictions, for the reason that the reconstruction result of a small region will be affected by its surrounding area in the receptive field. In Fig. 10(d), the DoP-based method overestimates the volume scattering. As we stated before, the DoP-based method is based on the assumption that the cross-polarized scattering is fully contributed by the depolarized wave. Depolarized power mainly originates from two scattering mechanisms: volume and surface scattering, and the volume scattering is usually estimated directly from the cross-pol scattering. Thus, if the depolarized power is directly assigned to the cross-polarized scattering, the surface scattering will also be assigned, making the cross-polarized scattering term overestimated, so as the volume scattering. The color of some pixels is blue in Fig. 10(a), which means that the surface scattering is dominant in the back scattering of the area corresponding to these pixels. However, the main backscattering in the forest area is volume scattering, as shown in Fig. 10(a). The QPRFCN assigns the scattering mechanism of these pixels to the entire forest area, which results in a complete deviation from the original scattering mechanism. However, for the reason that the  $1 \times 1$  convolutional layer does not enlarge the receptive field, the receptive field of the CV-DBCNN is far less than that of the QPRFCN; therefore, the reconstruction result of the CV-DBCNN is more accurate than that of the QPRFCN.

Finally, we compare the reconstruction effect of the LS estimator, QPRFCN, the DoP-based method, and the CV-DBCNN on the GF-3 data (Hulunbeier Grassland region), agriculture area (area A). Fig. 11 shows the scatter plots of the CV-DBCNN, which is more compact and closer to the diagonal line compared with the QPRFCN, the LS estimator, and the DoP-based method. Fig. 12(b) shows that the LS estimator overestimates the volume scattering, which makes the green color in Fig. 12(b) darker than that in Fig. 12(a). The reason is that in CP data with the  $\pi/4$  mode, the proportion of the volume scattering component is larger than that of quad-pol data, especially in the agriculture area. The reason is that the LS estimator is based on a three-component decomposition method, which will result in overestimation of the volume scattering in the pseudo quad-pol data. As shown

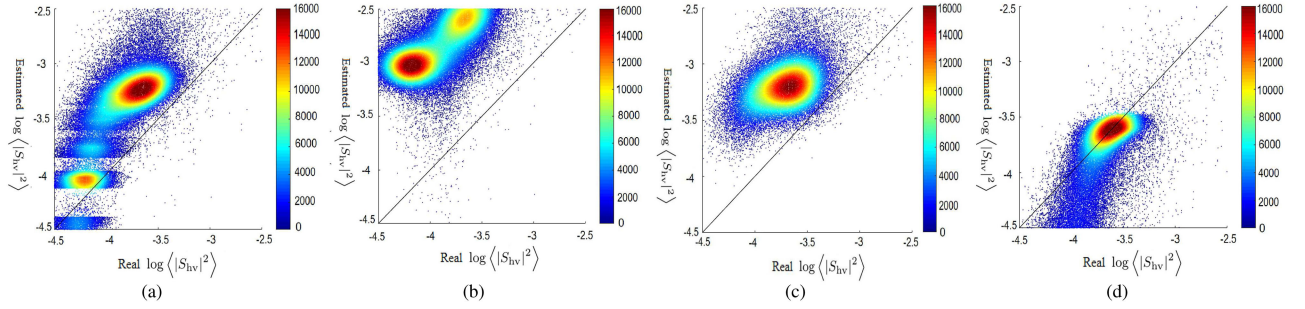


Fig. 7. Scatter plots of the estimated  $\log \langle |S_{hv}|^2 \rangle$  for the water area (area A) of UAVSAR testing data, the real value of  $\log \langle |S_{hv}|^2 \rangle$  is displayed on the abscissa, and the estimated value is displayed on the ordinate. (a) LS estimator. (b) QPRFCN. (c) DoP-based method. (d) CV-DBCNN.

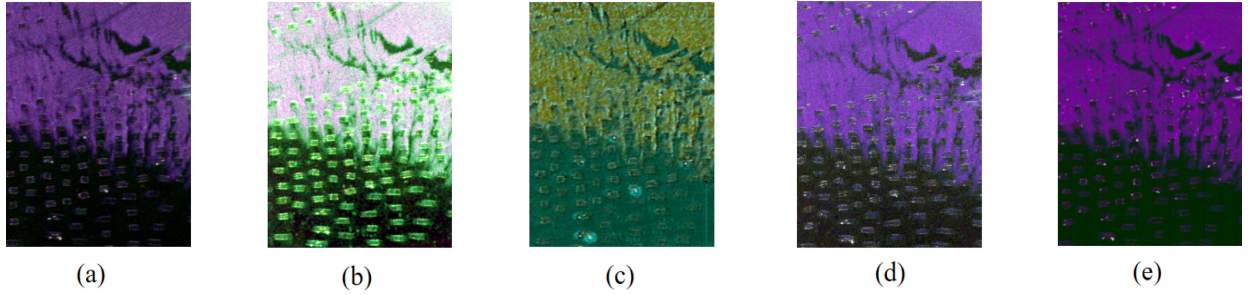


Fig. 8. Pauli-basis images of the reconstructed pseudo quad-pol data for the water area (area A) in UAVSAR testing data. (a) Real quad-pol data. (b) LS estimator. (c) QPRFCN. (d) DoP-based method. (e) CV-DBCNN. The red, green, and blue channels of the Pauli-basis image represent the double-bounce scattering, volume scattering, and single-bounce scattering, respectively.

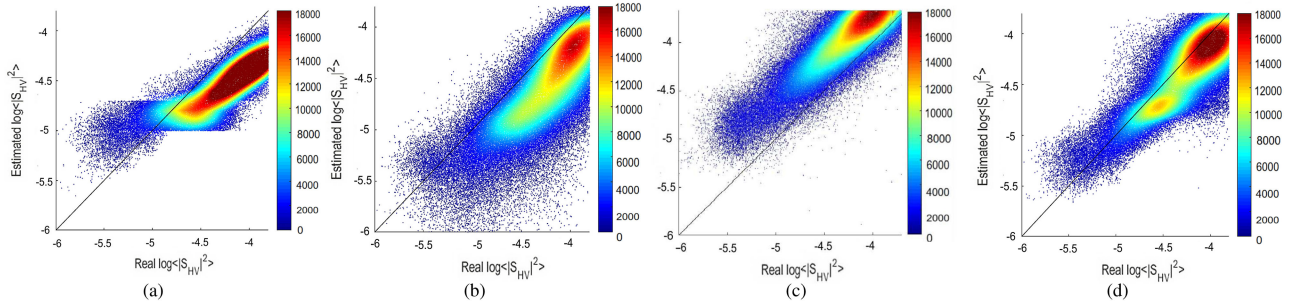


Fig. 9. Scatter plots of the estimated  $\log \langle |S_{hv}|^2 \rangle$  for the forest area (area A) in ESAR testing data, the real value of  $\log \langle |S_{hv}|^2 \rangle$  is displayed on the abscissa, and the estimated value is displayed on the ordinate. (a) LS estimator. (b) QPRFCN. (c) DoP-based method. (d) CV-DBCNN.

in Fig. 12(d), the DoP-based method overestimates the volume scattering, which is similar to the simulation result in the forest area of ESAR data. As shown in Fig. 12(a) and (e), the Pauli-basis image of the CV-DBCNN is consistent with that of real quad-pol data, which shows that the CV-DBCNN has better reconstruction effect than the QPRFCN and the LS estimator within the agriculture area.

In conclusion, the CV-DBCNN has more accurate reconstruction result than those of the LS estimator, the QPRFCN, and the DoP-based method from three simulated CP datasets with different sensors and different bands. Quantitative error analysis is shown in Table III. As shown in Table III, the CV-DBCNN is superior to the QPRFCN, the LS estimator, and the DoP-based method in two quantitative indicators. Besides, we replace the complex convolution layer and the

complex activation function in the CV-DBCNN with the ordinary convolution layer and the leaky ReLU activation function (DBCNN), in order to validate whether adding the complex convolution layer and the activation function can get better reconstruction effect. Obviously, the CV-DBCNN is superior to the DBCNN in both quantitative indicators. In particular, the COI of the CV-DBCNN is 10% higher than that of the DBCNN. For the LS estimator, its reconstruction performance is better than that of the QPRFCN on all three simulated CP datasets. However, the reconstruction accuracy of the LS estimator is lower than that of the CV-DBCNN. Moreover, the computational cost of the LS estimator is too large. For each pixel, the LS estimator needs to use the gradient descent method to find a local minimum in an interval, which is the value of the reconstructed cross-polarized term of the pixel. When the size of CP data is large, it results



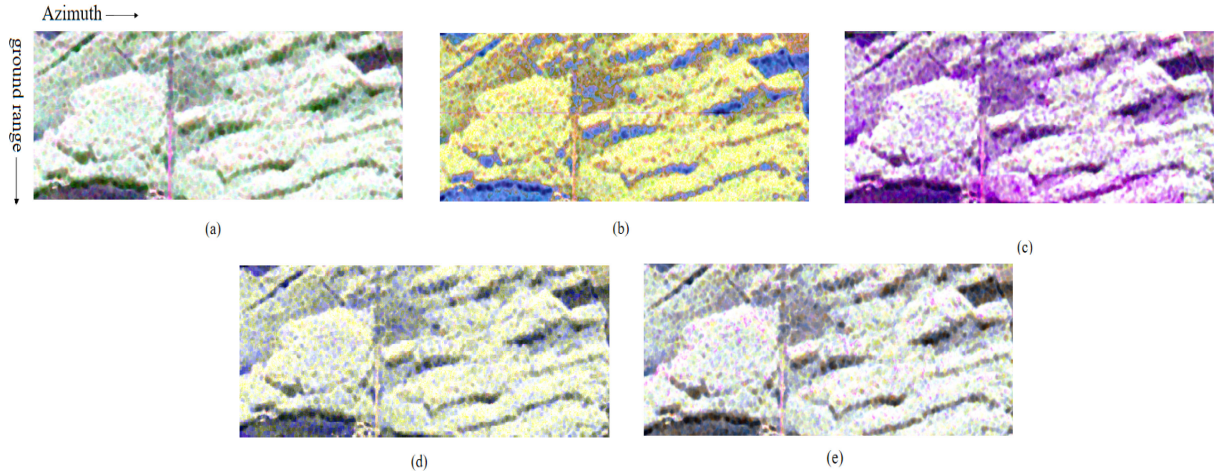


Fig. 10. Pauli-basis images of the reconstructed pseudo quad-pol data for the forest area (area A) in ESAR testing data. (a) Real quad-pol data. (b) LS estimator. (c) QPRFCN. (d) DoP-based method. (e) CV-DBCNN. The red, green, and blue channels of the Pauli-basis image represent the double-bounce scattering, volume scattering, and single-bounce scattering, respectively.

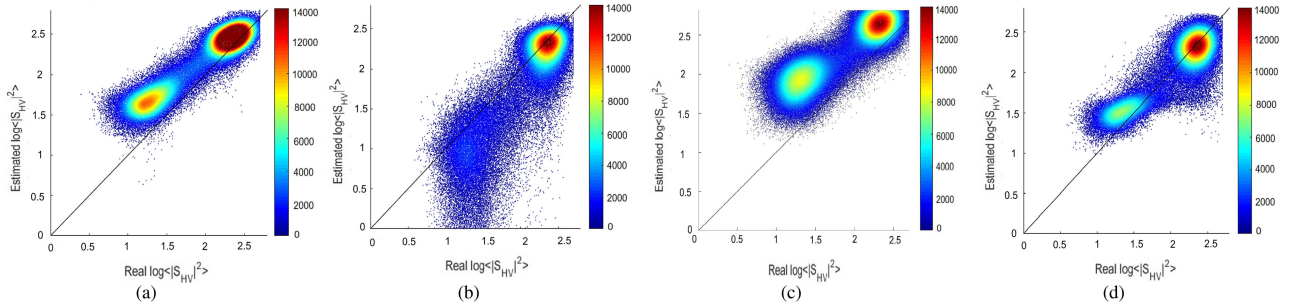


Fig. 11. Scatter plots of the estimated  $\log \langle |S_{HV}|^2 \rangle$  for agriculture area (area A) in GF-3 testing data, the real value of  $\log \langle |S_{HV}|^2 \rangle$  is displayed on the abscissa, and the estimated value is displayed on the ordinate. (a) LS estimator. (b) QPRFCN. (c) DoP-based method. (d) CV-DBCNN.

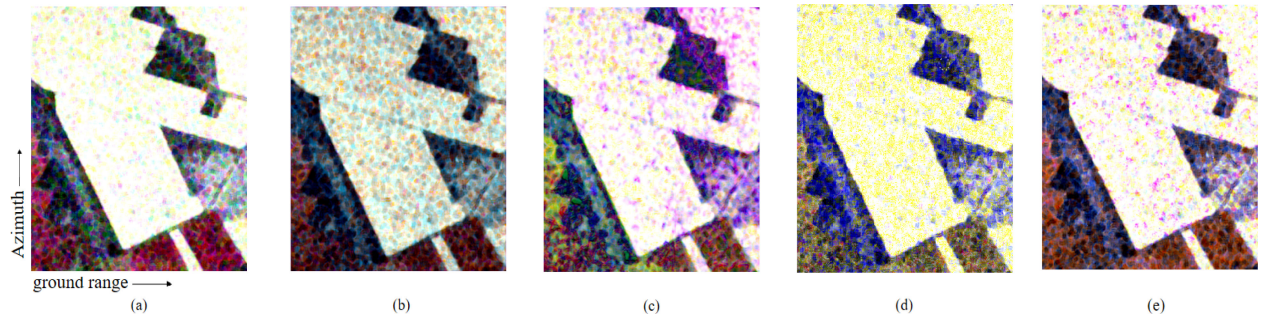


Fig. 12. Pauli-basis images of the reconstructed pseudo quad-pol data for the agriculture area (area A) in GF-3 testing data. (a) Real quad-pol data. (b) LS estimator. (c) QPRFCN. (d) DoP-based method. (e) CV-DBCNN. The red, green, and blue channels of the Pauli-basis image represent the double-bounce scattering, volume scattering, and single-bounce scattering, respectively.

in a huge amount of time cost (the time for the LS estimator to reconstruct an image with size of  $2000 \times 2000$  is about 45 h). For the reconstruction method based on deep learning, such as the QPRFCN and the CV-DBCNN, with a well-trained network, we can get the reconstruction result immediately instead of waiting for a long time. For the QPRFCN, its too deep network hierarchy leads to too large receptive field, which will make the reconstruction result seriously deviate from the real quad-pol

data. In contrast, the CV-DBCNN has a smaller receptive field and few parameters than the QPRFCN, making the network easier to converge and have better reconstruction performance than the QPRFCN. The experimental results indicate that the CV-DBCNN achieves better reconstruction effect than the three state-of-the-art methods (i.e., QPRFCN, LS estimator, and DoP-based method). In summary, the proposed CV-DBCNN has a stronger adaptability to the reconstruction of pseudo quad-pol



TABLE III  
QUANTITATIVE ERROR ANALYSIS

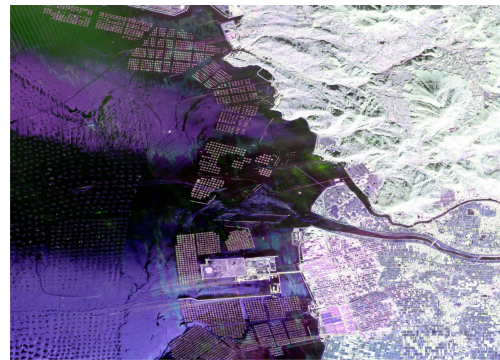
Data	Terrain Type	Metrics	LS Estimator	QPRFCN	DoP	DBCNN	CV-DBCNN
UAVSAR	Water	MAE	0.0774	0.0865	0.0462	0.0536	<b>0.0427</b>
		COI	0.695	0.724	0.910	0.811	<b>0.926</b>
ESAR	Forest	MAE	0.0797	0.0818	0.0844	0.0741	<b>0.0619</b>
		COI	0.604	0.596	0.764	0.753	<b>0.841</b>
GF-3	Farmland	MAE	0.0667	0.0613	0.0658	0.0559	<b>0.0532</b>
		COI	0.746	0.768	0.797	0.803	<b>0.884</b>

data from the CP data with different sensors and different bands and has better generalization performance than the QPRFCN, the LS estimator, and the DoP-based method.

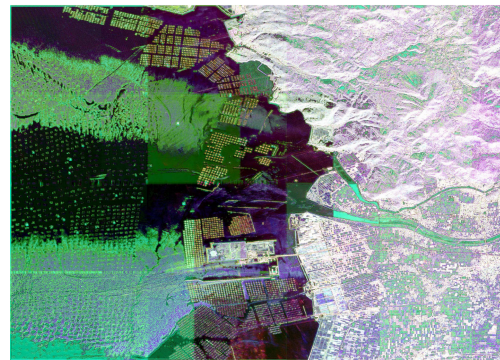
#### E. Comparison Results on the Entire CP Dataset With Different Methods

In the previous subsection, we completely compare the reconstruction performance of the LS estimator, the QPRFCN, the DoP-based method, and CV-DBCNN on different terrain types. The experimental results show that the CV-DBCNN performs better than the LS estimator, the QPRFCN, and the DoP-based method in terms of quantitative indicators, scatter plots, and visual results on three different terrain types. The DoP-based method is based on an assumption that the surface scattering exhibits zero response in the cross-polarized term, i.e., the depolarized power is totally contributed by the volume scattering. Therefore, the DoP-based method is suitable for the area such as the sea ice that satisfies this condition [23]. However, the depolarized power is contributed by both of the volume and surface scattering in many cases, and the cross-polarized power is mainly contributed by the volume scattering [23]. Thus, when the DoP-based method assigns all the depolarized power to the cross-polarized channel, it will lead to the overestimation of the cross-polarized scattering in most of nature areas. For the pseudo quad-pol data simulation by the DoP-based method, the volume scattering is overestimated and the surface scattering is underestimated, which are explained in the experimental results in Section IV-D. Due to the limitation of the DoP-based method, we do not conduct the comparison of the DoP-based method on the entire CP image. In addition, note that the time cost of the LS estimator to reconstruct all three testing datasets is too high; thus, here, we only further compare the reconstruction effects of the CV-DBCNN and the QPRFCN on the entire CP testing dataset, which mainly focus on the deep learning performance evaluation.

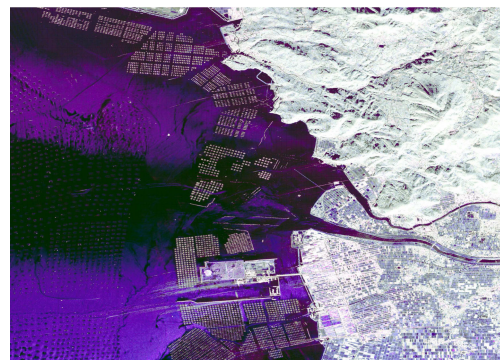
Fig. 13 shows the Pauli-basis images of the reconstructed pseudo quad-pol data with different methods for the entire UAVSAR quad-pol data. Fig. 13(a) shows that the UAVSAR data contain many different types of land covers, including water body, agriculture area, and forest area, which are densely distributed. In Fig. 13(b), the QPRFCN obviously overestimates the volume scattering within water area and overestimates the



(a)



(b)



(c)

Fig. 13. Pauli-basis images of the reconstructed pseudo quad-pol data with different methods (UAVSAR). (a) Real quad-pol data. (b) QPRFCN. (c) CV-DBCNN. The red, green, and blue channels of the Pauli-basis image represent the double-bounce scattering, volume scattering, and single-bounce scattering, respectively.

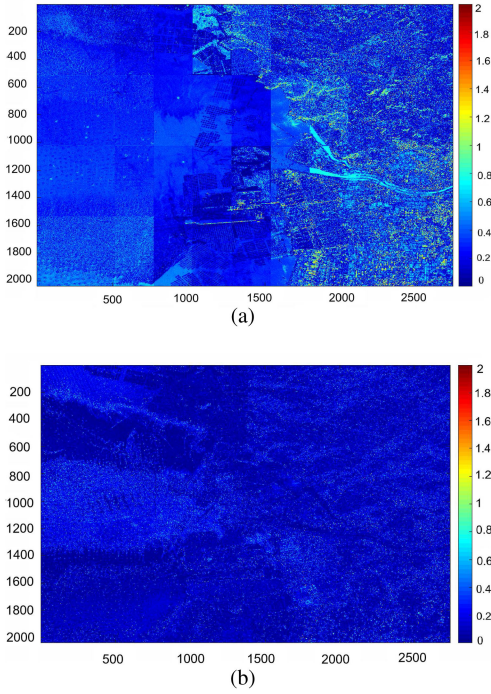


Fig. 14. Relative errors of the reconstructed  $\log \langle |S_{hv}|^2 \rangle_c$  for UAVSAR test data, where the relative error is defined by, e.g.,  $|\log \langle |S_{hv}|^2 \rangle_c - \log \langle |S_{hv}|^2 \rangle| / \log \langle |S_{hv}|^2 \rangle$ . The relative error of  $\log \langle |S_{hv}|^2 \rangle_c$  reconstructed by the QPRFCN and the CV-DBCNN, is shown in (a) and (b), respectively.

double-bounce scattering within agriculture area and forest area. However, the reconstruction result of the CV-DBCNN is consistent with the original quad-pol data in all kinds of land covers, as shown in Fig. 13(c). This indicates that the CV-DBCNN is more robust and has much better generalization performance than the QPRFCN. Besides, we can also observe that there is a difference of the terrain features between Fig. 13(a) and (c). Note that reconstruction from CP data to pseudo quad-pol data only changes the form of the CP data to the form of quad-pol data. The polarimetric information saved in the CP image does not change after the reconstruction, i.e., without increasing any new information. However, the polarimetric information saved by the CP image is less than that of the quad-pol image; the reconstructed pseudo quad-pol image will definitely lack some information than the real quad-pol image. Fig. 14 shows the relative error of the QPRFCN and the CV-DBCNN. As shown in Fig. 14(a) and (b), in the water area and agriculture area, the relative error of the QPRFCN is significantly higher than that of the CV-DBCNN. Fig. 15 gives the cross-polarized term of the UAVSAR data after averaging by columns. The cross-polarized term reconstructed by the QPRFCN obviously deviates the real value, whereas the reconstruction result of the CV-DBCNN is more close to the original cross-polarized term, as shown in Fig. 15(a) and (b). To further evaluate the scattering mechanism preservation between the real and reconstructed quad-pol data, we perform the Freeman three-component decomposition on the real and proposed reconstructed pseudo quad-pol data, respectively, and

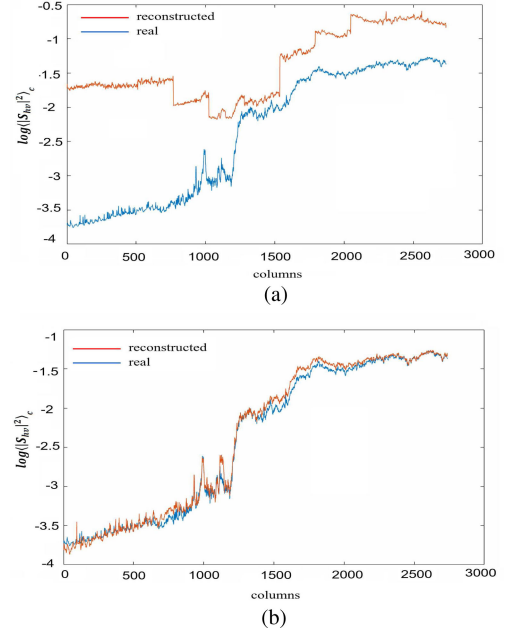


Fig. 15. Value of the reconstructed cross-polarized term after averaging by columns. (a) QPRFCN. (b) CV-DBCNN.

then give the proportions of double-bounce, odd-bounce, and volume scattering components. Fig. 16 shows the combined RGB images of the decomposition results in the water area of the UAVSAR data, where the red, green, and blue channels of the Pauli-basis image represent the double-bounce scattering, volume scattering, and surface scattering, respectively. Fig. 17 shows the proportions of double-bounce, odd-bounce, and volume scattering components in Fig. 16. From Figs. 16 and 17, we can find that in the water area of the original quad-pol data, odd-bounce scattering is dominant with some double-bounce scattering. The reconstructed pseudo quad-pol data have the similar scattering mechanisms. However, the volume scattering is overestimated, as shown in Figs. 16(b) and 17(b). The overestimation of the volume scattering is inevitable for the reason that the ratio of volume scattering of CP data is higher than that of quad-pol data. Fig. 18 shows the combined decomposition images of the urban area of the UAVSAR data. Fig. 19 shows the proportions of three scattering components. We can see through Figs. 18(b) and 19(b) that the CV-DBCNN overestimates the volume component in the urban area for the reason that the reflection symmetry is not fully satisfied the urban area, which will influence the reconstruction from CP data to quad-pol data. However, it is worth pointing out that the double-bounce scattering is still the dominate scattering in the urban area of the pseudo quad-pol data, which consists of the radar polarimetric scattering behavior. Above all, in Figs. 17 and 19, the reconstructed pseudo quad-pol data and the real quad-pol data have the similar scattering mechanisms. However, the volume scattering is overestimated due to the higher ratio of volume scattering of CP data than that of quad-pol data. The reason is that the scattering of some areas does not obey the reflection symmetry. Therefore, the volume scattering overestimation will

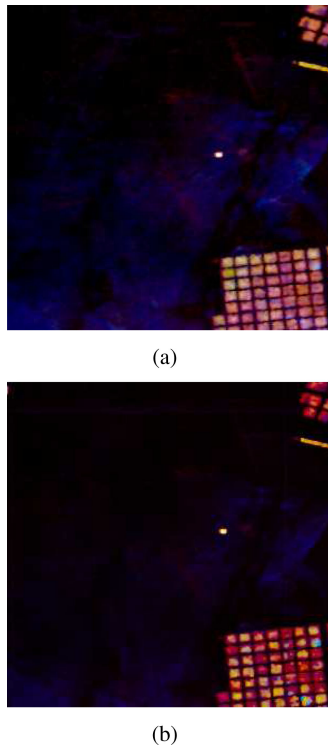


Fig. 16. Combined RGB image of the three-component decomposition for UAVSAR data (Ocean area). The red, green, and blue channels of the Pauli-basis image represent the double-bounce scattering, volume scattering, and single-bounce scattering, respectively. (a) Decomposition results of the real quad-pol data. (b) Decomposition results of the reconstructed quad-pol data.

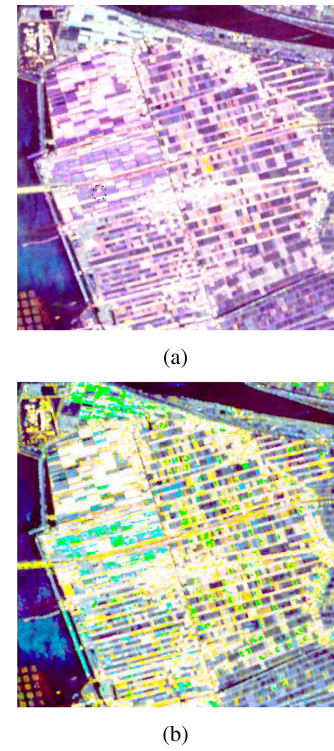


Fig. 18. Combined RGB image of the three-component decomposition for UAVSAR data (Urban area). The red, green, and blue channels of the Pauli-basis image represent the double-bounce scattering, volume scattering, and single-bounce scattering, respectively. (a) Decomposition results of the real quad-pol data. (b) Decomposition results of the reconstructed quad-pol data.

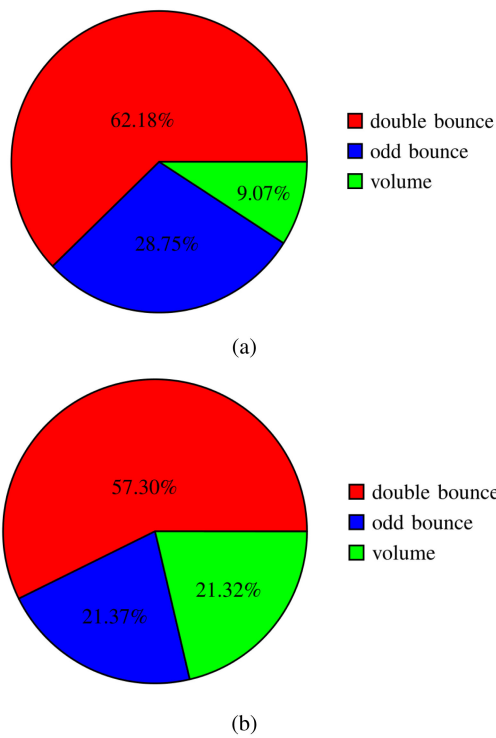


Fig. 17. Proportions of double-bounce, odd-bounce, and volume scattering components in the ocean area of UAVSAR data. (a) Results of the real quad-pol data. (b) Results of the reconstructed quad-pol data.

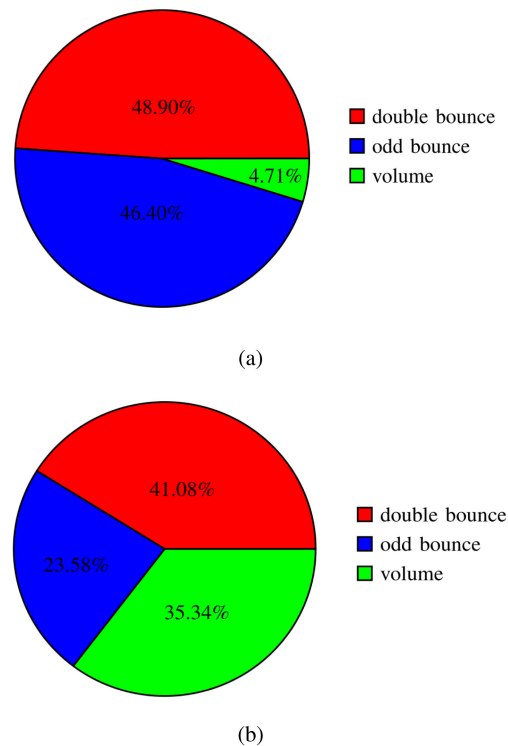


Fig. 19. Proportions of double-bounce, odd-bounce, and volume scattering components in the urban area of UAVSAR data. (a) Results of the real quad-pol data. (b) Results of the reconstructed quad-pol data.





Fig. 20. Pauli-basis images of the reconstructed pseudo quad-pol data with different methods (GF-3). (a) Real quad-pol data. (b) QPRFCN. (c) CV-DBCNN. The red, green, and blue channels of the Pauli-basis image represent the double-bounce scattering, volume scattering, and single-bounce scattering, respectively.

exist in our proposed method. However, the dominate scattering mechanism will not change in comparison with the real quad-pol data.

The Pauli-basis images of quad-pol GF-3 data are shown in Fig. 20, and the relative error of the reconstructed  $\log \langle |S_{hv}|^2 \rangle_c$  reconstructed by the QPRFCN and the CV-DBCNN is shown in Fig. 21. Similar to UAVSAR data, the QPRFCN seriously

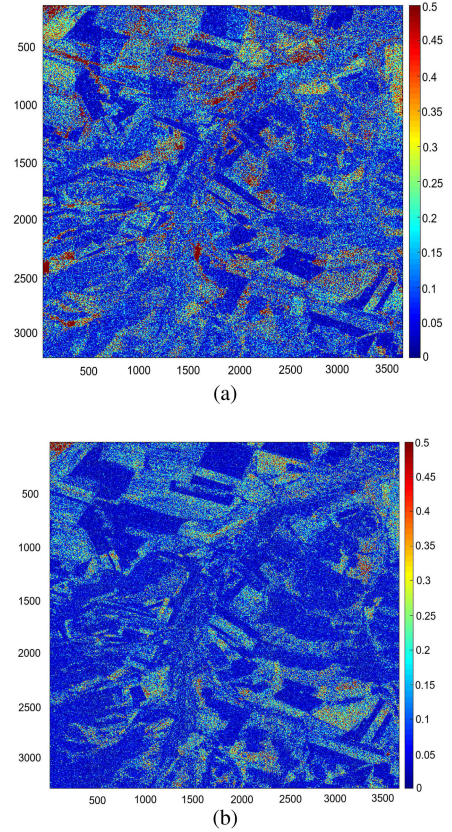


Fig. 21. Relative errors of the reconstructed  $\log \langle |S_{hv}|^2 \rangle_c$  for GF-3 test data. The relative error of  $\log \langle |S_{hv}|^2 \rangle_c$  reconstructed by the QPRFCN and the CV-DBCNN is shown in (a) and (b), respectively.

overestimates the volume scattering on GF-3 data, especially in the agriculture area, whereas the CV-DBCNN achieves more accurate reconstruction results.

Fig. 22 shows the Pauli-basis images of different reconstruction methods for the ESAR quad-pol data. As shown in Fig. 22(a), the ESAR testing data contain two main terrain types: forest area and urban area. Fig. 22(b) and (c) shows that the reconstruction result of the QPRFCN is inconsistent with the original quad-pol data, especially in the forest area. However, the color of the CV-DBCNN is more accurate than the QPRFCN. Besides, the scattering mechanism preservation ability of reconstruction methods is important. In this article, we introduce the  $H/\alpha$  decomposition to further analyze the ability of the QPRFCN and the CV-DBCNN on the preservation of the scattering mechanisms.

$H/\alpha$  decomposition [44] is a classical method for scattering mechanism analysis. Fig. 23(a) shows the  $H/\alpha$  decomposition scattering plot diagram of real quad-pol ESAR data (Munich area,  $L$ -band). Fig. 23(b) and (c) shows the decomposition results of the pseudo quad-pol data reconstructed by the QPRFCN and the CV-DBCNN. As shown in Fig. 23(a), the  $H/\alpha$  decomposition results of the real quad-pol data indicate that in ESAR data, high-entropy vegetation scattering, medium-entropy multiple scattering, and medium-entropy vegetation scattering are dominant. The high-entropy vegetation



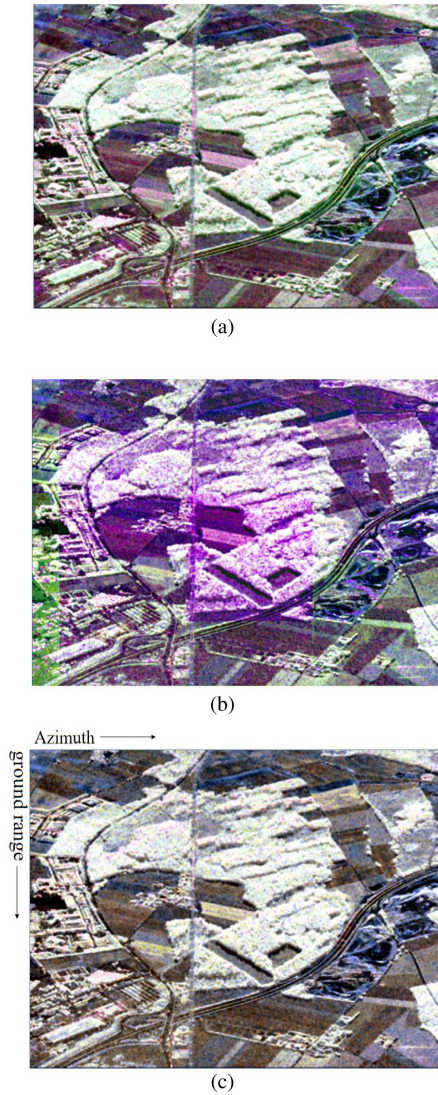


Fig. 22. Pauli-basis images of the reconstructed pseudo quad-pol data with different methods (ESAR). (a) Real quad-pol data. (b) QPRFCN. (c) CV-DBCNN. The red, green, and blue channels of the Pauli-basis image represent the double-bounce scattering, volume scattering, and single-bounce scattering, respectively.

scattering includes the scattering of forest canopy. The medium-entropy multiple scattering may occur in the forest area and the urban area. The medium-entropy vegetation scattering mainly occurs on the vegetation areas composed of anisotropic and moderately correlated direction angle scatterers. It is shown in Fig. 23(b) and (c) that the decomposition results of the CV-DBCNN are more closer to the decomposition results of real quad-pol data than the QPRFCN. The QPRFCN overestimates the medium-entropy vegetation scattering and underestimates the high-entropy vegetation scattering, as shown in Fig. 23(b). Above all, the ability of the CV-DBCNN on the preservation of the scattering mechanism is stronger than that of the QPRFCN.

The polarimetric decomposition result of the ESAR data is shown in Figs. 24 and 25. Fig. 24(a) shows the  $\alpha$  decomposition result of the original quad-pol data, Fig. 24(b) shows the  $\alpha$  decomposition result of the QPRFCN, and Fig. 24(c) shows

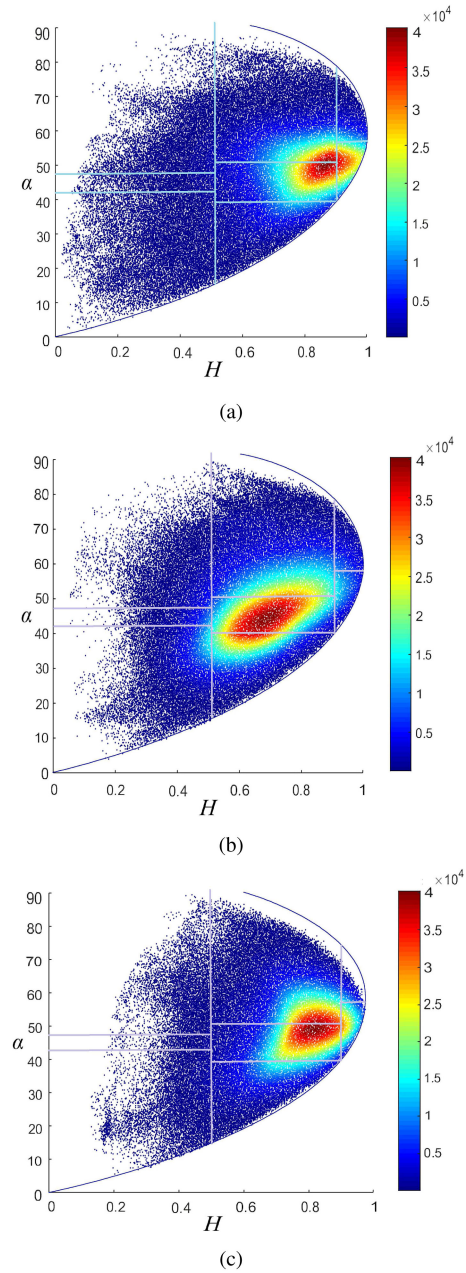


Fig. 23.  $H/\alpha$  decomposition scattering plots diagrams of the ESAR data (Munich area,  $L$ -band).  $H$  (entropy) is displayed on the abscissa and  $\alpha$  is displayed on the ordinate. (a) Decomposition results of the original quad-pol data. (b) Decomposition results of the QPRFCN. (c) Decomposition results of the CV-DBCNN estimator.

the  $\alpha$  decomposition result of the proposed CV-DBCNN. In the city area of ESAR data, as shown in areas A and B of Fig. 24(a), we can clearly observe that the result of the QPRFCN is obviously deviate from the  $\alpha$  decomposition result of the original quad-pol data. However, the  $\alpha$  decomposition result of the CV-DBCNN is more closer to the true value. The entropy decomposition result of the original quad-pol data is shown in Fig. 25(a), Fig. 25(b) shows the result of the QPRFCN, and Fig. 25(c) shows the result of the proposed CV-DBCNN. It is clear that the QPRFCN seriously underestimates the entropy of



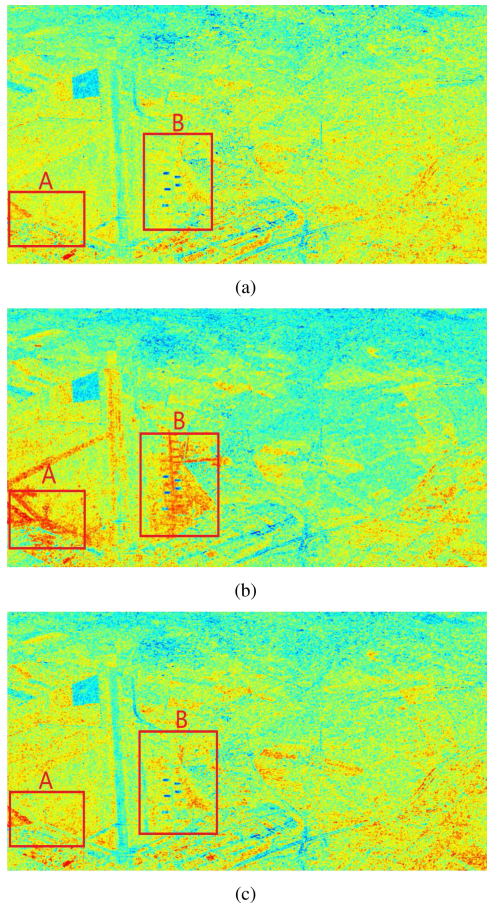


Fig. 24.  $\alpha$  of the  $H/\alpha$  decomposition results of the ESAR data (Munich area, L-band). Areas A and B are different part of the city area in ESAR data. (a)  $\alpha$  decomposition result of the original quad-pol data. (b)  $\alpha$  decomposition result of the QPRFCN. (c)  $\alpha$  decomposition result of CV-DBCNN estimator.

the forest area of ESAR data, which can be seen in area A of Fig. 25(a), whereas the result of the CV-DBCNN is more closer to the real value, as shown in Fig. 25(b) and (c).

## V. CONCLUSION

In this article, we proposed a method to reconstruct the pseudo quad-pol data from CP data. This method was based on a CV-DBCNN, which consists of the branch with  $1 \times 1$  kernel size and the branch with  $3 \times 3$  kernel size. The proposed network can learn the regional polarimetric features of the training data and generate the nonlinear combination relationships between the channels of the input CP data.

Compared with the three state-of-the-art method (i.e., QPRFCN, LS estimator, and DoP-based method), our method showed a superior performance in both quantitative error analysis and scatter plots, especially in the result of the  $H/\alpha$  decomposition, which shows that the reconstructed pseudo quad-pol data of the proposed method has better preservation capacity of the scattering mechanisms than that of other methods. In the future, we will focus on the extension of our method on the pseudo quad-pol data reconstruction from CP data with

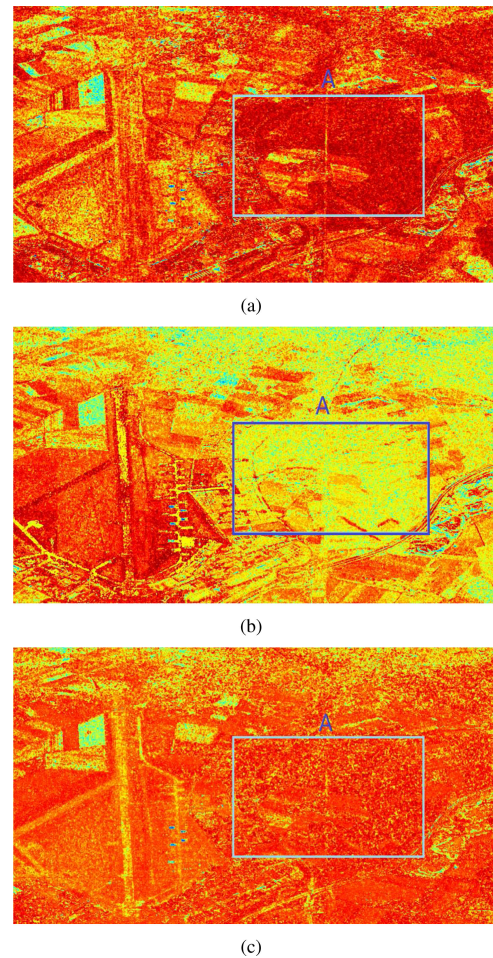


Fig. 25. Entropy ( $H$ ) of the  $H/\alpha$  decomposition results of the ESAR data (Munich area, L-band). Area A is the forest area of the ESAR data. (a) Entropy decomposition result of the original quad-pol data. (b) Entropy decomposition result of the QPRFCN. (c) Entropy decomposition result of the CV-DBCNN estimator.

the DCP and HCP modes and validation with real CP data. Besides, the assumption of reflection symmetry is not always true for different land covers, which would also limit the scope of application of our proposed method. In the future, we will explore other assumptions, which are more universal than the reflection symmetry.

## REFERENCES

- [1] A. Moreira, P. Prats-Iraola, M. Younis, G. Krieger, I. Hajnsek, and K. P. Papathanassiou, "A tutorial on synthetic aperture radar," *IEEE Geosci. Remote Sens. Mag.*, vol. 1, no. 1, pp. 6–43, Mar. 2013.
- [2] J. C. Souyris, P. Imbo, R. Fjortoft, S. Mingot, and J. S. Lee, "Compact polarimetry based on symmetry properties of geophysical media: The  $\pi/4$  mode," *IEEE Trans. Geosci. Remote Sens.*, vol. 43, no. 3, pp. 634–646, Mar. 2005.
- [3] R. K. Raney, "Hybrid-polarity SAR architecture," *IEEE Trans. Geosci. Remote Sens.*, vol. 45, no. 11, pp. 3397–3404, Nov. 2007.
- [4] F. J. Charbonneau *et al.*, "Compact polarimetry overview and applications assessment," *Can. J. Remote Sens.*, vol. 36, no. Sup2, pp. S 298–S315, 2010.
- [5] N. Stacy and M. Preiss, "Compact polarimetric analysis of X-band SAR data," in *Proc. 6th Eur. Conf. Synth. Aperture Radar*, Dresden, Germany: VDE Verlag GMBH, 2006.



- [6] M. Dabboor and T. Geldsetzer, "Towards sea ice classification using simulated RADARSAT constellation mission compact polarimetric SAR imagery," *Remote Sens. Environ.*, vol. 140, pp. 189–195, 2014.
- [7] V. Turkar, S. De, Y. S. Rao, S. Shitole, A. Bhattacharya, and A. Das, "Comparative analysis of classification accuracy for RISAT-1 compact polarimetric data for various land-covers," in *Proc. IEEE Int. Geosci. Remote Sens. Symp.*, 2013, pp. 3586–3589.
- [8] C. Lardeux, P. L. Frison, C. Tison, D. Deleflie, and B. Stoll, "Comparison of compact polarimetric with full polarimetric radar data for land use discrimination based on SVM classification," in *Proc. Int. Workshop Sci. Appl. SAR Polarimetry Polarimetric Interferometry*, 2007, Art. no. 19.
- [9] L. Chen, F. Cao, and W. Hong, "Unsupervised classification for compact polarimetric SAR data using  $m$ - $\delta$  decomposition, SPAN and the Wishart classifier," in *Proc. 2nd Asian-Pacific Conf. Synth. Aperture Radar*, 2009, pp. 742–745.
- [10] B. Zhang, X. Li, W. Perrie, and O. Garcia-Pineda, "Compact polarimetric synthetic aperture radar for marine oil platform and slick detection," *IEEE Trans. Geosci. Remote Sens.*, vol. 55, no. 3, pp. 1407–1423, Mar. 2017.
- [11] M. Ghanbari, D. A. Clausi, L. Xu, and M. Jiang, "Contextual classification of sea-ice types using compact polarimetric SAR data," *IEEE Trans. Geosci. Remote Sens.*, vol. 57, no. 10, pp. 7476–7491, Oct. 2019.
- [12] M. Ohki and M. Shimada, "Large-area land use and land cover classification with quad, compact, and dual polarization SAR data by PALSAR-2," *IEEE Trans. Geosci. Remote Sens.*, vol. 56, no. 9, pp. 5550–5557, Sep. 2018.
- [13] R. Shirvany, M. Chabert, and J.-Y. Tourneret, "Ship and oil-spill detection using the degree of polarization in linear and hybrid/compact dual-pol SAR," *IEEE J. Sel. Topics Appl. Earth Observ. Remote Sens.*, vol. 5, no. 3, pp. 885–892, Jun. 2012.
- [14] Z. Yang, Y. Shao, K. Li, Q. Liu, L. Liu, and B. Brisco, "An improved scheme for rice phenology estimation based on time-series multispectral HJ-1A/B and polarimetric RADARSAT-2 data," *Remote Sens. Environ.*, vol. 195, pp. 184–201, 2017.
- [15] F. Nunziata, M. Migliaccio, and X. Li, "Sea oil slick observation using hybrid-polarity SAR architecture," *IEEE J. Ocean. Eng.*, vol. 40, no. 2, pp. 426–440, Apr. 2015.
- [16] F. Charbonneau *et al.*, "Compact polarimetry: Multi-thematic evaluation," in *Proc. 4th Int. Workshop Sci. Appl. SAR Polarimetry Polarimetric Interferometry PolInSAR*, 2009, pp. 26–30.
- [17] R. Raney *et al.*, "The M-chi decomposition of hybrid dual-polarimetric radar data with application to lunar craters," *J. Geophys. Res., Planets*, vol. 117, no. E12, 2012.
- [18] K. Han, M. Jiang, M. Wang, and G. Liu, "Compact polarimetric SAR interferometry target decomposition with the Freeman–Durden method," *IEEE J. Sel. Topics Appl. Earth Observ. Remote Sens.*, vol. 11, no. 8, pp. 2847–2861, Aug. 2018.
- [19] A. Freeman and S. L. Durden, "A three-component scattering model for polarimetric SAR data," *IEEE Trans. Geosci. Remote Sens.*, vol. 36, no. 3, pp. 963–973, May 1998.
- [20] M. Nord, T. Ainsworth, J.-S. Lee, and N. Stacy, "Comparison of compact polarimetric synthetic aperture radar modes," *IEEE Trans. Geosci. Remote Sens.*, vol. 47, no. 1, pp. 174–188, Jan. 2009.
- [21] M. J. Collins, M. Denbina, and G. Atteia, "On the reconstruction of quad-pol SAR data from compact polarimetry data for ocean target detection," *IEEE Trans. Geosci. Remote Sens.*, vol. 51, no. 1, pp. 591–600, Jan. 2013.
- [22] Y. Li, Y. Zhang, J. Chen, and H. Zhang, "Improved compact polarimetric SAR quad-pol reconstruction algorithm for oil spill detection," *IEEE Geosci. Remote Sens. Lett.*, vol. 11, no. 6, pp. 1139–1142, Jun. 2014.
- [23] M. M. Espeseth, C. Brekke, and S. N. Anfinsen, "Hybrid-polarity and reconstruction methods for sea ice with L- and C-band SAR," *IEEE Geosci. Remote Sens. Lett.*, vol. 13, no. 3, pp. 467–471, Feb. 2016.
- [24] D. X. Yue, F. Xu, and Y. Q. Jin, "Wishart-Bayesian reconstruction of quad-pol from compact-pol SAR image," *IEEE Geosci. Remote Sens. Lett.*, vol. 14, no. 9, pp. 1623–1627, Sep. 2017.
- [25] J. Yin, W. Moon, and J. Yang, "Model-based pseudo-quad-pol reconstruction from compact polarimetry and its application to oil-spill observation," *J. Sens.*, vol. 2015, 2015, Art. no. 734848.
- [26] A. Freeman, "Fitting a two-component scattering model to polarimetric SAR data from forests," *IEEE Trans. Geosci. Remote Sens.*, vol. 45, no. 8, pp. 2583–2592, Aug. 2007.
- [27] J. Yin, K. P. Papathanassiou, J. Yang, and P. Chen, "Least-squares estimation for pseudo quad-pol image reconstruction from linear compact polarimetric SAR," *IEEE J. Sel. Topics Appl. Earth Observ. Remote Sens.*, vol. 12, no. 10, pp. 3746–3758, Oct. 2019.
- [28] Q. Yin, J. Cheng, F. Zhang, Y. Zhou, L. Shao, and W. Hong, "Interpretable POLSAR image classification based on adaptive-dimension feature space decision tree," *IEEE Access*, vol. 8, pp. 173826–173837, 2020.
- [29] Y. Li, X. Li, Q. Sun, and Q. Dong, "SAR image classification using CNN embeddings and metric learning," *IEEE Geosci. Remote Sens. Lett.*, vol. 19, 2022, Art no. 4002305.
- [30] H. Dong, B. Zou, L. Zhang, and S. Zhang, "Automatic design of CNNs via differentiable neural architecture search for PolSAR image classification," *IEEE Trans. Geosci. Remote Sens.*, vol. 58, no. 9, pp. 6362–6375, Sep. 2020.
- [31] F. M. Bianchi, M. M. Espeseth, and N. Borch, "Large-scale detection and categorization of oil spills from SAR images with deep learning," *Remote Sens.*, vol. 12, no. 14, 2020, Art. no. 2260.
- [32] Y. Li, S. Zhang, and W.-Q. Wang, "A lightweight faster R-CNN for ship detection in SAR images," *IEEE Geosci. Remote Sens. Lett.*, vol. 19, 2022, Art no. 4006105.
- [33] A. B. Campos, M. I. Pettersson, V. T. Vu, and R. Machado, "False alarm reduction in wavelength-resolution SAR change detection schemes by using a convolutional neural network," *IEEE Geosci. Remote Sens. Lett.*, vol. 19, 2022, Art no. 4004805.
- [34] R. Li, X. Wang, J. Song, and L. Lei, "SAR target recognition based on efficient fully convolutional attention block CNN," *IEEE Geosci. Remote Sens. Lett.*, vol. 19, 2022, Art no. 4005905.
- [35] D. Xiang *et al.*, "Adaptive statistical superpixel merging with edge penalty for PolSAR image segmentation," *IEEE Trans. Geosci. Remote Sens.*, vol. 58, no. 4, pp. 2412–2429, Apr. 2020.
- [36] Z. Lin, K. Ji, X. Leng, and G. Kuang, "Squeeze and excitation rank faster R-CNN for ship detection in SAR images," *IEEE Geosci. Remote Sens. Lett.*, vol. 16, no. 5, pp. 751–755, May 2019.
- [37] F. I. Alam *et al.*, "Conditional random field and deep feature learning for hyperspectral image classification," *IEEE Trans. Geosci. Remote Sens.*, vol. 57, no. 3, pp. 1612–1628, Mar. 2019.
- [38] Q. Song, F. Xu, and Y. Q. Jin, "Radar image colorization: Converting single-polarization to fully polarimetric using deep neural networks," *IEEE Access*, vol. 6, pp. 1647–1661, 2018.
- [39] F. Gu, H. Zhang, and C. Wang, "Quad-pol reconstruction from compact polarimetry using a fully convolutional network," *Remote Sens. Lett.*, vol. 11, no. 4, pp. 397–406, 2020.
- [40] A. Hirose, *Complex-Valued Neural Networks: Advances and Applications*. Hoboken, NJ, USA: Wiley, 2013.
- [41] Z. Zhang, H. Wang, F. Xu, and Y. Jin, "Complex-valued convolutional neural network and its application in polarimetric SAR image classification," *IEEE Trans. Geosci. Remote Sens.*, vol. 55, no. 12, pp. 7717–7188, Dec. 2017.
- [42] R. K. Raney, B. Brisco, M. Dabboor, and M. Mahdianpari, "RADARSAT constellation missions operational polarimetric modes: A user-driven radar architecture," *Can. J. Remote Sens.*, vol. 47, no. 1, pp. 1–16, 2021.
- [43] J. Geng, W. Jiang, and X. Deng, "Multi-scale deep feature learning network with bilateral filtering for SAR image classification," *ISPRS J. Photogramm. Remote Sens.*, vol. 167, pp. 201–213, 2020.
- [44] S. Cloude and E. Pottier, "An entropy based classification scheme for land applications of polarimetric SAR," *IEEE Trans. Geosci. Remote Sens.*, vol. 35, no. 1, pp. 68–78, Jan. 1997.



**Fan Zhang** (Senior Member, IEEE) received the B.E. degree in communication engineering from the Civil Aviation University of China, Tianjin, China, in 2002, the M.S. degree in signal and information processing from Beihang University, Beijing, China, in 2005, and the Ph.D. degree in signal and information processing from the Institute of Electronics, Chinese Academy of Sciences, Beijing, in 2008.

He is currently a Full Professor of Electronic and Information Engineering with the Beijing University of Chemical Technology, Beijing. His research interests include remote sensing image processing, high-performance computing, and artificial intelligence.

Dr. Zhang is an Associate Editor for IEEE ACCESS and a Reviewer for IEEE TRANSACTIONS ON GEOSCIENCE AND REMOTE SENSING, IEEE JOURNAL OF SELECTED TOPICS IN APPLIED EARTH OBSERVATIONS AND REMOTE SENSING, IEEE GEOSCIENCE AND REMOTE SENSING LETTERS, and *Journal of Radars*.

**Zhuoyue Cao** received the B.S. degree in electronic science and technology in 2019 from the Beijing University of Chemical Technology, Beijing, China, where he is currently working toward the M.S. degree in computer science and technology with the College of Information Science and Technology.

His research interests include machine learning and synthetic aperture radar image target detection.



**Deliang Xiang** received the B.S. degree in remote sensing science and technology from Wuhan University, Wuhan, China, in 2010, the M.S. degree in photogrammetry and remote sensing from the National University of Defense Technology, Changsha, China, in 2012, and the Ph.D. degree in geoinformatics from the KTH Royal Institute of Technology, Stockholm, Sweden, in 2016.

He has been a Full Professor with Interdisciplinary Research Center for Artificial Intelligence, Beijing University of Chemical Technology, Beijing, China,

since 2020. His research interests include urban remote sensing, synthetic aperture radar (SAR)/polarimetric SAR image processing, artificial intelligence, and pattern recognition.

Dr. Xiang received a Humboldt Research Fellowship in 2019. He is a Reviewer for *Remote Sensing of Environment*, *ISPRS Journal of Photogrammetry and Remote Sensing*, *IEEE TRANSACTIONS ON GEOSCIENCE AND REMOTE SENSING*, *IEEE JOURNAL OF SELECTED TOPICS IN APPLIED EARTH OBSERVATIONS AND REMOTE SENSING*, *IEEE GEOSCIENCE AND REMOTE SENSING LETTERS*, and several other international journals in the remote sensing field.

**Canbin Hu** received the B.S., M.S., and Ph.D. degrees in information and communication engineering from the National University of Defense Technology, Changsha, China in 2006, 2008, and 2014, respectively.

He has been a Lecturer with the College of Information Science and Technology, Beijing University of Chemical Technology, Beijing, China, since 2021. His research interests include synthetic aperture radar (SAR)/polarimetric SAR image processing and pattern recognition.

**Fei Ma** received the B.S., M.S., and Ph.D. degrees in electronic and information engineering from the Beijing University of Aeronautics and Astronautics, Beijing, China, in 2013, 2016, and 2020, respectively.

He was a Research Fellow with the Department of Electrical Engineering, McGill University, Montreal, QC, Canada, from 2017 to 2018. He has been a Full Associate Professor with the College of Information Science and Technology, Beijing University of Chemical Technology, Beijing, since 2020. His research interests include synthetic aperture radar image processing, machine learning, artificial intelligence, and target detection.

**Qiang Yin** (Member, IEEE) received the B.S. degree in electronic and information engineering from the Beijing University of Chemical Technology, Beijing, China, in 2004, and the M.S. and Ph.D. degrees in signal and information processing from the Institute of Electronics, Chinese Academy of Science, Beijing, in 2008 and 2016, respectively.

She was a Research Assistant with the Institute of Electronics, Chinese Academy of Sciences, from 2008 to 2013. She was a Research Fellow with the European Space Agency, Roma, Italy, from 2014 to 2015. She is currently an Associate Professor with the College of Information Science and Technology, Beijing University of Chemical Technology. Her research interests include polarimetric/polarimetric interferometric synthetic aperture radar processing and applications.

**Yongsheng Zhou** (Member, IEEE) received the B.E. degree in communication engineering from Beijing Information Science and Technology University, Beijing, China, in 2005, and the Ph.D. degree in signal and information processing from the Institute of Electronics, Chinese Academy of Sciences, Beijing, in 2010.

He is currently a Professor of Electronic and Information Engineering with the College of Information Science and Technology, Beijing University of Chemical Technology, Beijing. His research interests include target detection and recognition from microwave remotely sensed image and digital signal and image processing.